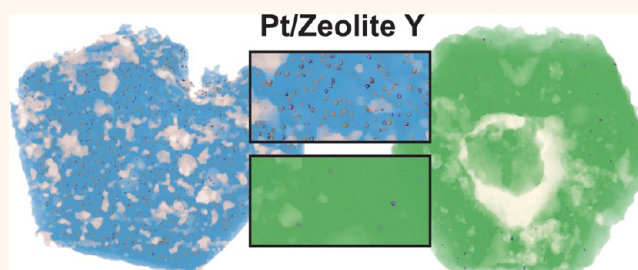# Heterogeneities of the Nanostructure of Platinum/Zeolite Y Catalysts Revealed by Electron Tomography

Jovana Zečević,[†] Ad M. J. van der Eerden,[†] Heiner Friedrich,[‡] Petra E. de Jongh,[†] and Krijn P. de Jong[†,*]

[†]Inorganic Chemistry and Catalysis, Debye Institute for Nanomaterials Science, Utrecht University, Universiteitsweg 99, 3584 CG Utrecht, The Netherlands and
[‡]Laboratory of Materials and Interface Chemistry, Department of Chemical Engineering and Chemistry, Eindhoven University of Technology, Den Dolech 2, 5612 AZ Eindhoven, The Netherlands

ABSTRACT To develop structure—performance relationships for important catalysts, a detailed characterization of their morphology is essential. Using electron tomography, we determined in three dimensions the structure of Pt/zeolite Y bifunctional catalysts. Optimum experimental conditions enabled for the first time high-resolution 3D imaging of Pt particles as small as 1 nm located inside zeolite micropores. Semiautomated image analysis of 3D reconstructions provided an efficient study of numbers, size distributions, and interparticle distances of thousands of Pt particles within individual zeolite crystals. Upon extending this approach to a number of zeolite crystals of one batch of Pt/zeolite Y catalyst, heterogeneities were revealed. The Pt loading, an important parameter for catalyst performance, varied between zeolite crystals up to a factor of 35. This discovery calls for re-evaluation of catalyst preparation methods and suggests potential for lowering the nominal loading with noble metals.

Bifunctional zeolite-supported Pt or Pd catalysts are important for the hydrogenation process in oil refineries[1−5] and are also a potential candidate for hydrodesulfurization of oil fractions.[6−10] Bifunctionality stems from metal nanoparticles enabling (de)hydrogenation of hydrocarbons and zeolite acid sites performing cracking/isomerization of hydrogenated species. Next to the requirement of a high dispersion of the metal nanoparticles, the concentration, ratio, and proximity of active metal sites and zeolite acid sites are important for achieving a balance between the two functions and consequently optimizing catalyst performance.[11−14] In that respect, metal nanoparticles should be located inside the microporous zeolite framework close to the acid sites. A great effort has been made to design highly dispersed and homogeneously distributed supported metal particles, and studies were performed to elucidate the evolution of Pt or Pd nanoparticles and the influence of impregnation and heat treatment conditions on particle size, distribution, and location during the catalyst

preparation.[15−22] Commonly, these studies employ bulk characterization techniques such as extended X-ray absorption fine structure (EXAFS) and H_2 (or CO) chemisorption to determine the size of the metal nanoparticles.[15,16,19,20] This means that in the case of measuring 100 mg of a 1 wt % Pt-loaded support containing 1 nm metal particles, one averages over $\sim 10^{16}$ particles. Heterogeneities in solid catalysts have been studied using advanced micro- and nanospectroscopic tools with micrometer or tens of nanometer resolution.[23] Transmission electron microscopy (TEM), in particular, high-resolution (HR)TEM, offers local information with nanometer or even angstrom resolution about shapes and sizes of metal nanoparticles and an overview of the support morphology.[15,18] Nevertheless, the determination of the location and exact sizes of these metal nanoparticles is restricted by the lack of third dimension in common (HR)TEM micrographs, where sample features are projected onto a 2D plane. Electron tomography (ET, also known as 3D-TEM) has been successfully
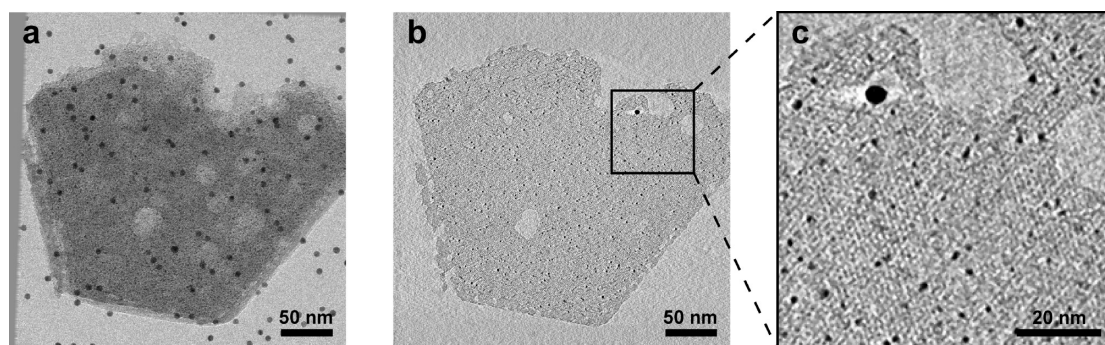
Figure 1. Electron tomography study of a Pt-HY30 crystal. (a) TEM at 0° tilt angle; black dots are 5 nm gold particles used for the alignment of the tilt images, while very small black dots inside the zeolite crystal are Pt particles; (b) 0.32 nm thick reconstructed volume slice from the middle of the same zeolite crystal confirming the presence of Pt particles inside the crystal. (c) Detail of (b) showing the presence of very small Pt nanoparticles as well as the zeolite crystal lattice periodicity. White streaks emerging from the sides of the larger Pt particle in (c) are artifacts of the reconstruction and should not be confused with the presence of a mesopore.

employed in studying morphological properties of various materials in three dimensions. It was introduced in the field of materials science more than a decade ago by Koster et al.,[24] and due to the significance of the information ET provides, the number of studies rapidly expanded.[24−41] Three-dimensional reconstructions obtained from ET can be submitted to image analysis. This enables (semi)automated segmentation of features of interest, such as zeolite or SBA mesopores,[33,38] nanoparticles on and in carbon nanotubes[25,34] or porous oxide supports,[35] and qualitative and quantitative assessment of their properties. This approach results in more reliable and objective processing of a larger amount of information when compared to labor-intensive manual tracing and measurement of particles.

Here we employ electron tomography and image analysis as a powerful tool to reveal quantitative nanoscale features that are inaccessible to other techniques. Optimal imaging conditions resulted in the unique opportunity to visualize in three dimensions thousands of Pt particles as small as 1 nm located inside zeolite micropores and to qualitatively and quantitatively study morphological differences between various Pt/zeolite crystals. Variations in Pt loading between zeolite crystals were observed for the first time, as well as the tendency of zeolite crystals to accommodate Pt particles exceeding the size of the micropores. Additionally, Pt particle sizes were compared with average particle sizes determined by EXAFS.

RESULTS AND DISCUSSION

Zeolite Y is a well-known and widely used aluminosilicate support, having an interconnected network of micropores (with so-called supercages of 1.2 nm diameter) and acid sites located at the surface of the micropore walls. In order to increase mass transport through the crystals, mesopores (2−50 nm) are commonly introduced by steaming and acid leaching.[42−45] In this study, we used a mesoporous zeolite Y sample that

was in the H-form and had a Si/Al atomic ratio of 30, hence we refer to it as HY30. The size distribution, shape, and accessibility of HY30 mesopores were investigated in detail in a previous study,[38] and the textural properties of HY30 are covered in section 2 of the Supporting Information. To obtain a bifunctional zeolite-supported Pt catalyst with highly dispersed Pt particles, impregnation of zeolite HY30 powder and following heat treatments were performed as described previously.[15,16] This includes calcination in air flow at approximately 350 °C with a low heating ramp (0.5 °C/min) as a crucial step for the formation of small Pt/PtO_x particles and subsequent reduction in H_2 or H_2/N_2 gas flow to obtain metallic Pt. In addition, we investigated the influence of a slight increase in the reduction temperature (from 600 to 650 °C) on the Pt dispersion.

TEM revealed (Figure 1a and Supporting Information Figure S1) that, irrespective of the reduction temperature, samples contained well-dispersed 1−2 nm Pt particles (dark spots) which seem to be well-distributed across the crystals, while lighter regions of the crystals imply the presence of the mesopores. Upon detailed analysis of micrographs, some zeolite crystals appeared to contain more Pt particles than others. Due to the two-dimensional nature of the micrographs, it is impossible to ascertain the 3D location of these Pt particles. Hence, we submitted this crystal to electron tomography (ET) with multiple TEM images taken from different directions and used to reconstruct the crystal by back-projecting the information (see experimental section of the Supporting Information). This results in a reconstructed volume, that is, a set of thin (in this study 0.2−0.32 nm) cross sections which can be viewed and processed individually. One such cross section (Figure 1b) depicts the inside of the crystal without interference with features above or below the plane of view. It is now evident that the Pt particles are indeed well-distributed throughout the zeolite crystal (see the Supporting Information movie 1 showing the whole reconstructed volume) and ∼1−2 nm in diameter,

close to the size of the zeolite Y micropore cavities. Moreover, optimal imaging conditions of this rather thin zeolite crystal resulted in a high-resolution reconstruction revealing the periodicity of the crystal lattice (Figure 1c). The hypothesis that Pt particles are formed inside zeolite supercages was postulated decades ago;[22] however, to the best of our knowledge, the first direct confirmation is offered by this electron tomography study. Reconstructing zeolite crystals and resolving small metal nanoparticles is a challenging task, particularly in the case of imaging lower-Z metals (e.g., Ni, Cu) in oxide supports which limits the contrast. Furthermore, most of the zeolites are susceptible to electron beam damage which can negatively influence the resolution of the reconstruction. To avoid this, a low electron dose is mandatory which, on the other hand, can reduce the contrast between zeolite crystal and metal particles, particularly for structures more than 400 nm in thickness. As can be seen in earlier study by Philippaerts et al.,[46] these factors limit the resolution, and Pt particles smaller than 2 nm could not be resolved. An alternative approach is to image consecutive ultrathin sections (∼20 nm) of a zeolite crystal cut by ultramicrotomy.[47] However, this technique is destructive and can introduce artifacts originating from physical sectioning.

An interesting phenomenon observed by electron tomography (Figure 1) is the high density of Pt particles, pointing to a higher Pt loading that nominal 1 wt % in this particular zeolite particle. To investigate this, we extended our research to three other zeolite crystals of the same Pt-HY30 sample. In Figure 2, the first three rows show TEM images and slices from the reconstructions of all examined crystals. It is clear that the density of Pt particles varies, especially when comparing crystals in Figure 2a,d. Nevertheless, the Pt particles seem to be similar in size (1−2 nm) and uniformly distributed throughout the volumes of all imaged zeolite crystals (see row 3 of Figure 2 for zoomed-in regions of reconstruction slices).

Since manual tracking and measuring thousands of Pt particles is demanding and susceptible to errors, reconstructed volumes were subjected to semiautomated image analysis, particularly suitable for systems with high contrast between metal nanoparticles and support. First, median-filtered reconstructed volumes were segmented to identify Pt particles, zeolite mesopores, and microporous zeolite region, by applying different threshold values (see experimental section of the Supporting Information for a detailed description). Volume and isosurface rendering of the segmented features offers insight into the morphology of the crystals (Figure 2, row 4). On the basis of the volumes of segmented Pt particles and zeolite crystals, Pt loadings of individual zeolite crystals were calculated. A significant variation in loading between different crystals, already suggested by the TEM and ET images,

is confirmed by this quantitative approach (Figure 2, row 4). Up to a 7-fold higher than nominal (1 wt %) Pt loading is calculated for the crystal in Figure 2a, and crystals in Figure 2b,c have near nominal loading, while the crystal 2d is loaded with only 0.2 wt % Pt. Please note that in order to preserve the zeolite from electron beam damage experiments were performed under low electron doses which resulted in decreased contrast between zeolite crystals and mesopores. This might further impair the precision of zeolite segmentation and calculation of related Pt loadings; however, the loading variation is unambiguous (Figure 3). Here we speculate that possible causes of loading variation might be either heterogeneous distribution of Pt species upon zeolite impregnation or a variation in the Si/Al ratio of pristine zeolite crystals. In the latter case, differences in Al content and, hence, Brønsted acidity of individual zeolite crystals could influence the amount of $Pt(NH_3)_4^{2+}$ exchanged with protons at the acid sites. This discovery calls for re-evaluation of catalyst preparation methods, and it also implies potential for lowering the nominal loading of noble metals if a more uniform distribution can be realized.

The segmented Pt particles were also indexed to isolate the volumes of individual Pt particles and calculate their diameters assuming a spherical shape. The size distribution of thousands of Pt particles within the four different zeolite crystals is shown in row 5 of Figure 2. The distribution curves are narrow with mean Pt diameters of 1−1.5 nm, which is close to the size of the zeolite supercages. A slight variation in mean Pt diameter among the crystals can be attributed to the different magnifications at which the crystals were imaged; the higher the magnification, the smaller the Pt particle size that can be resolved. The fact that Pt particles retain their size even in the case of very highly loaded zeolite crystals points to a pronounced stabilization of the particles by the zeolite supercages at the given heat treatment conditions. Also, nearest neighbor Pt−Pt distances were derived (row 6 of Figure 2), which are of particular interest when studying metal nanoparticle growth.[41] Since the Pt particles do not significantly vary in size, nearest neighbor distances are strongly related to the Pt loading of the zeolite crystals.

Somewhat larger (∼3 nm) Pt particles are occasionally observed (e.g., in Figure 1c). To study the size and location of these larger Pt particles, we prepared a Pt-HY30-R sample by drying it and submitting it to direct reduction in H₂, which promotes Pt growth. Figure 4 shows that the Pt particles in the Pt-HY30-R sample are now ∼3 nm in diameter and well-distributed throughout the whole volume of the zeolite crystal (Supporting Information movie 2). Interestingly, the majority of the particles appear to be entrapped inside the zeolite crystal, while the large mesopores are mostly empty. One of the possibilities is that the
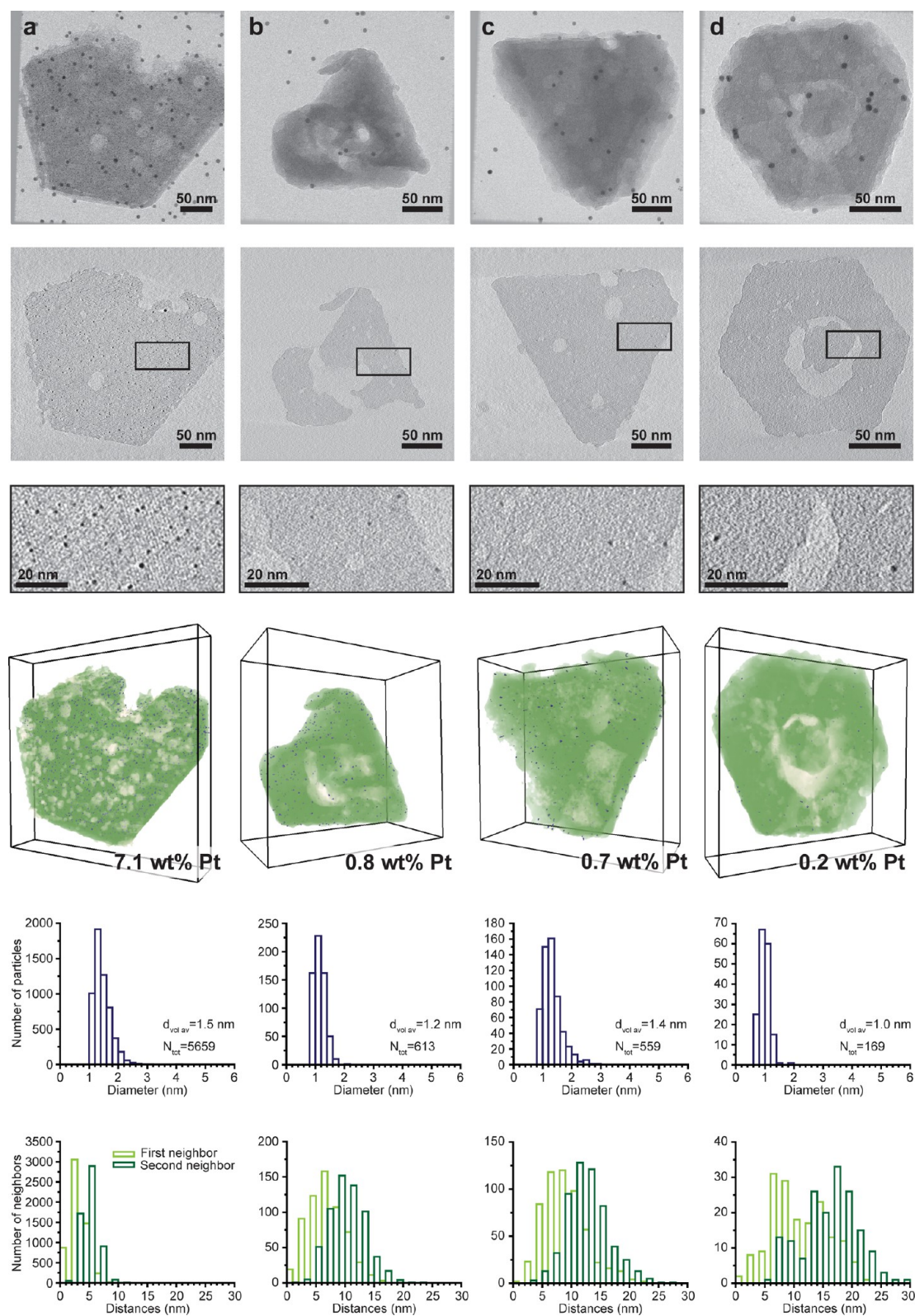
Figure 2. Electron tomography and image analysis of various Pt-HY30 crystals recorded at 50 000× (a), 62 000× (b,c), and 80 000× (d) magnification. In the first row, TEM micrographs taken at 0° tilt angle are shown. In the second and third rows, 0.32 nm (a), 0.26 nm (b,c), and 0.20 nm (d) thick slices through the reconstructed volumes and details thereof are shown. In the fourth row, volume and isosurface-rendered representations of crystals with Pt loadings (wt %) derived from image analysis are shown, with zeolite crystals in green, Pt particles in blue, and mesopores in white. Pt size distributions, volume-averaged Pt diameters, and total number of measured particles are shown in row 5. Surface-to-surface distances of the first and the second nearest neighboring Pt particles are presented in row 6.
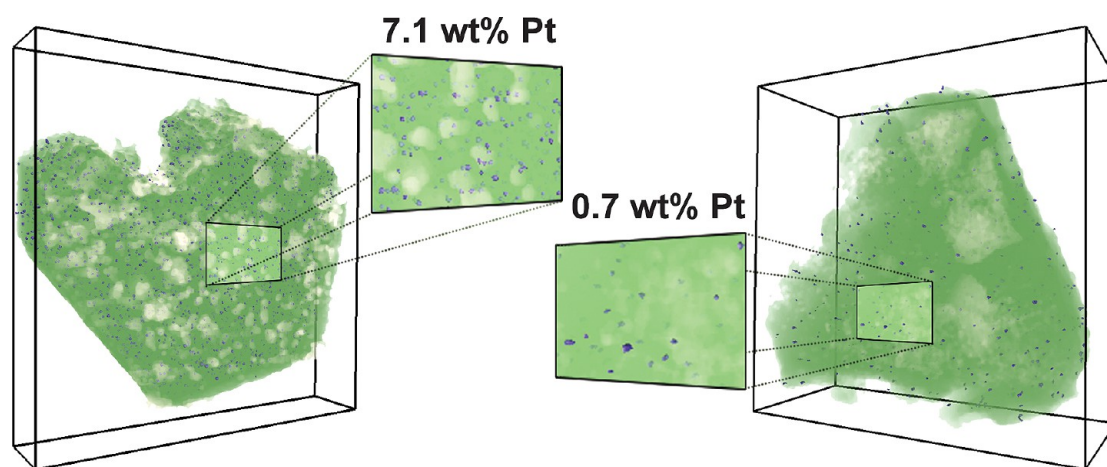
Figure 3. Difference in Pt loading between two Pt-HY30 crystals from Figure 2. Regions of the rendered volumes are selected to highlight the variation in Pt loading that occurs.
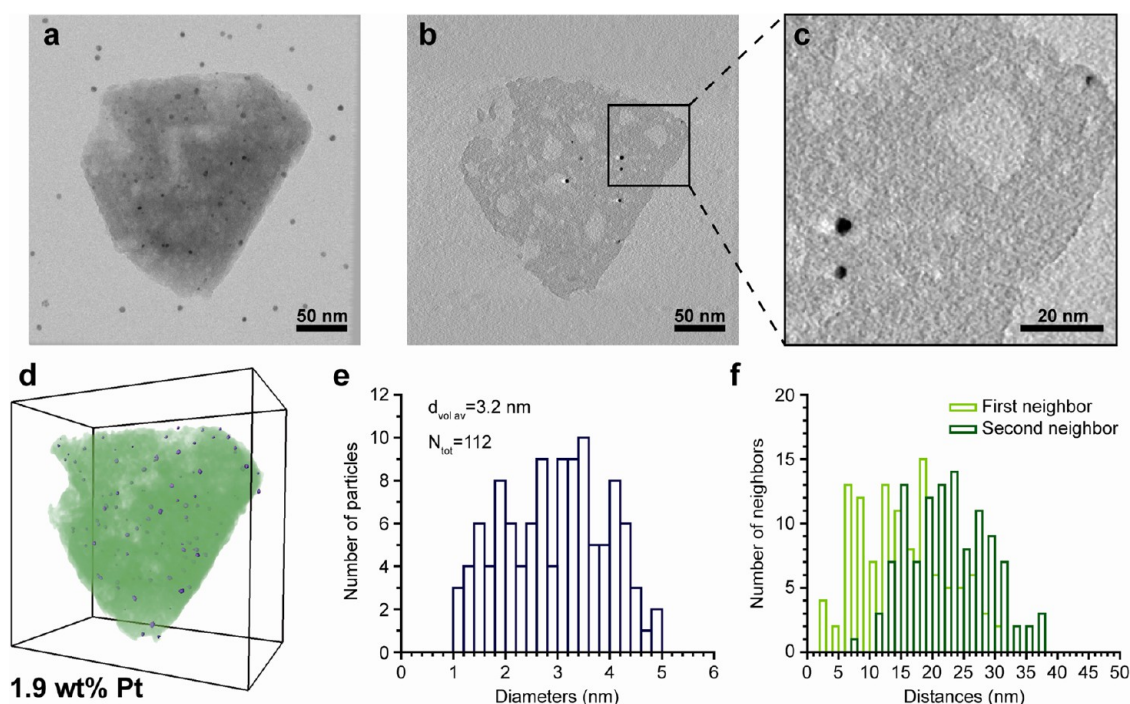

Figure 4. Electron tomography and image analysis study of a Pt-HY30-R crystal. (a) TEM at 0° tilt angle; black dots are 5 nm gold particles used for the alignment of the tilt images; (b) 0.32 nm thick reconstruction slice from the middle of the zeolite crystal shown in (a). (c) Enlarged region (b) highlighting the presence of larger Pt particles. White streaks emerging from the Pt particles are artifacts of the weighted back-projection reconstruction and should not be confused with the presence of mesopores. (d) Volume and isosurface rendering shows segmented Pt particles (blue), zeolite crystal (green), and mesopores (white). (e) Pt size distribution, volume-averaged Pt diameter, and total number of measured Pt particles. (f) Surface-to-surface distances of first and second nearest neighbor Pt particles.

Pt particles are located in small mesopore cavities of similar size which can be found in this support.[38,45] However, an additional experiment in which nonmesoporous HY zeolite was used showed that even in the absence of mesopores large Pt particles are located inside the zeolite crystal (see section 3 of the Supporting Information). This implies that the growth of the Pt particles is accompanied by a local destruction of the zeolite micropore network leading to the formation of small cavities (~3.5 nm) that accommodate these

larger particles.[15,19] Local properties of the zeolite Y network possibly favor the creation of defects of this characteristic size since small (~3 nm) mesopores also emerged upon base leaching of HY30.[45] Moreover, the observed uniform distribution of Pt particles in non-mesoporous zeolite crystals points to the fact that mesopore accessibility is not a critical factor in the Pt deposition under the employed conditions. Reconstruction of Pt-HY30-R and image analysis (Figure 4d−f) yielded a somewhat broader Pt size distribution, with

a volume-averaged Pt diameter of 3.2 nm. When compared to our recent study,[48] where Pt growth was promoted by using a H_2PtCl_6 precursor and the Pt size distribution was bimodal (1−2 nm Pt and 3−4 nm Pt), here almost all of the Pt particles seem to be ~3 nm. Nearest neighbor Pt−Pt distances (Figure 4f) are higher than that in the Pt-HY30 sample since the number of Pt particles inside the zeolite crystal is relatively low.

An additional set of experiments was carried out in order to investigate whether the loading variation phenomenon was also observed after slightly different sample preparation (section 4 of the Supporting Information). Pt-impregnated HY30 powders were pelletized, crushed, and sieved prior to calcination and reduction treatment. Supporting Information Figures S2 and S3 show ET and image segmentation results, which point to a similar morphology as in the case of Pt-HY30 and Pt-HY30-R powdered samples. Large variations in Pt loading were again present, while ICP confirmed average loadings of ~1 wt % for both samples. Narrow Pt size distributions were observed (Supporting Information Figure S4), suggesting a positive effect of pelletizing samples prior to heat treatment. EXAFS measurements yielded 0.9 and 2.0 nm Pt diameters, which is in good agreement with the volume-averaged Pt diameters in the range of 0.9−1.2 and 1.8−2.1 nm for the pelletized forms of Pt-HY30 and Pt-HY30-R samples, respectively.

CONCLUSIONS

Electron tomography and image analysis were successfully applied for a detailed qualitative and quantitative analysis of the structure of bifunctional Pt-supported zeolite Y catalysts. Optimum imaging conditions enabled visualization of thousands of small Pt particles (~1 nm) residing inside the zeolite Y micropores. By studying individual zeolite crystals, it was revealed that the Pt loading varied dramatically from crystal to crystal (up to factor of 35). In the case of hydrocracking, for which the relative amount of metal and acid active sites and their vicinity play a crucial role in product selectivity, these heterogeneities of Pt loading at the level of individual crystals might be an important factor for macroscale catalyst performance. Determining the cause of and preventing this variation is yet to be investigated. However, it suggests that part of the Pt is not used optimally, especially in the zeolite crystals containing much more Pt than average. This discovery implies potential for lowering the nominal loading of noble metals by realizing a more uniform distribution. Despite the Pt loading variations, in all of the analyzed crystals, the Pt size distribution was narrow with a mean Pt diameter of 1−1.5 nm, which is close to the size of the micropores. Even for Pt particle diameters of 3−4 nm, particles remained inside the micropore system, pointing to a collapse of neighboring micropores upon particle growth. This study clearly shows that morphological differences can appear at the level of individual zeolite crystals. Hence quantitative local analysis, for which the combination of electron tomography and image analysis is a powerful tool, should complement average bulk characterization to understand structure−performance relationships in complex structures such as bifunctional catalysts.

MATERIALS AND METHODS

Chemicals. USY zeolite ("Ultra Stable Y") in H-form with Si/Al = 30 was purchased from Zeolyst under the sample code CBV760. $Pt(NH_3)_4(NO_3)_2$ (99.995% purity) was purchased from Sigma Aldrich.

Synthesis. Mesoporous USY zeolite, to which we refer as HY30, was vacuum-dried overnight prior to incipient wetness impregnation. An appropriate volume of aqueous $Pt(NH_3)_4(NO_3)_2$ solution was added to fill 90% of total pore volume of HY30 (determined by N_2 physisorption as the sum of micropore and mesopore volumes). The nominal Pt loading was 1 wt %. Impregnated powder was dried in an oven at 60 °C for 1−3 h and left at 120 °C overnight, after which the sample was calcined at 350 °C for 2 h (with a ramp of 0.5 °C/min) in a plug-flow reactor under air flow (~5000 GHSV). The calcined sample was reduced in a flow of pure H_2 for 3 h at either 600 or 650 °C with a ramp of 5 °C/min. The final samples were referred to as Pt-HY30.

If after drying, the sample was placed in a plug flow reactor and submitted directly to reduction with pure H_2 flow for 3 h at 600 °C with a heating ramp of 5 °C/min, the obtained sample was referred to as Pt-HY30-R.

TEM, Electron Tomography, and Image Analysis. TEM imaging was performed on a Tecnai 12 (FEI, 120 kV) transmission electron microscope. Electron tomography experiments were performed on a Tecnai 20 (FEI) transmission electron microscope operated at 200 kV in bright-field imaging mode. Tilt images were aligned to a common origin and rotation axis by tracking 5 nm Au particles, binned by a factor 2, and then submitted to 3D reconstruction using a WBP (weighted back-projection) algorithm in IMOD.[49] Image analysis was performed in Matlab using the DipLib toolbox (www.diplib.org). Volume and isosurface rendering resulting in interactive color representations of segmented volumes were performed using Amira software. Variations in the segmentation threshold will vary the segmented mean Pt particle size. Therefore, EXAFS was performed to have an independent measurement on an even larger (~10^{16}) number of Pt particles which matches perfectly the ET results.

presented in section 3. In section 4, the influence of the pelletizing of the powders prior to heat treatments on Pt size distribution and Pt loading is discussed with accompanying EXAFS and ICP measurement results. Additional figures (S1–S4) and movies (1–2) are provided in sections 5 and 6. This material is available free of charge *via* the Internet at http://pubs.acs.org.

REFERENCES AND NOTES

1. Weitkamp, J. Catalytic Hydrocracking—Mechanisms and Versatility of the Process. *ChemCatChem* **2012**, *4*, 292–306.
2. Soualah, A.; Lemberton, J. L.; Pinard, L.; Chater, M.; Magnoux, P.; Moljord, K. Hydroisomerization of Long-Chain *n*-Alkanes on Bifunctional Pt/Zeolite Catalysts: Effect of the Zeolite Structure on the Product Selectivity and on the Reaction Mechanism. *Appl. Catal., A* **2008**, *336*, 23–28.
3. Arribas, M. A.; Martínez, A. The Influence of Zeolite Acidity for the Coupled Hydrogenation and Ring Opening of 1-Methylnaphthalene on Pt/USY Catalysts. *Appl. Catal., A* **2002**, *230*, 203–217.
4. Martens, G. G.; Marin, G. B.; Martens, J. A.; Jacobs, P. A.; Baron, G. V. A Fundamental Kinetic Model for Hydrocracking of C_8 to C_{12} Alkanes on Pt/US-Y Zeolites. *J. Catal.* **2000**, *195*, 253–267.
5. Park, K.-C.; Ihm, S.-K. Comparison of Pt/Zeolite Catalysts for *n*-Hexadecane Hydroisomerization. *Appl. Catal., A* **2000**, *203*, 201–209.
6. Zhang, L.; Fu, W.; Ke, Q.; Zhang, S.; Jin, H.; Hu, J.; Wang, S.; Tang, T. Study of Hydrodesulfurization of 4,6-DM-DBT over Pd Supported on Mesoporous USY Zeolite. *Appl. Catal., A* **2012**, *433−434*, 251–257.
7. Fu, W.; Zhang, L.; Tang, T.; Ke, Q.; Wang, S.; Hu, J.; Fang, G.; Li, J.; Xiao, F.-S. Extraordinarily High Activity in the Hydrodesulfurization of 4,6-Dimethyldibenzothiophene over Pd Supported on Mesoporous Zeolite Y. *J. Am. Chem. Soc.* **2011**, *133*, 15346–15349.
8. Sun, Y.; Wang, H.; Prins, R. Hydrodesulfurization with Classic Co−MoS$_2$ and Ni−MoS$_2$/γ-Al$_2$O$_3$ and New Pt−Pd on Mesoporous Zeolite Catalysts. *Catal. Today* **2010**, *150*, 213–217.
9. Ismagilov, Z. R.; Yashnik, S. A.; Startsev, A. N.; Boronin, A. I.; Stadnichenko, A. I.; Kriventsov, V. V.; Kasztelan, S.; Guillaume, D.; Makkee, M.; Moulijn, J. A. Deep Desulphurization of Diesel Fuels on Bifunctional Monolithic Nanostructured Pt-Zeolite Catalysts. *Catal. Today* **2009**, *144*, 235–250.
10. Sun, Y.; Prins, R. Hydrodesulfurization of 4,6-Dimethyldibenzothiophene over Noble Metals Supported on Mesoporous Zeolites. *Angew. Chem., Int. Ed.* **2008**, *47*, 8478–8481.
11. Francis, J.; Guillon, E.; Bats, N.; Pichon, C.; Corma, A.; Simon, L. J. Design of Improved Hydrocracking Catalysts by Increasing the Proximity between Acid and Metallic Sites. *Appl. Catal., A* **2011**, *409−410*, 140–147.
12. Thybaut, J. W.; Narasimhan, C. S. L.; Denayer, J. F.; Baron, G. V.; Jacobs, P. A.; Martens, J. A.; Marin, G. B. Acid−Metal Balance of a Hydrocracking Catalyst: Ideal *versus* Nonideal Behavior. *Ind. Eng. Chem. Res.* **2005**, *44*, 5159–5169.
13. Wang, J.; Li, Q.; Yao, J. The Effect of Metal−Acid Balance in Pt-Loading Dealuminated Y Zeolite Catalysts on the Hydrogenation of Benzene. *Appl. Catal., A* **1999**, *184*, 181–188.
14. Alvarez, F.; Ribeiro, F. R.; Perot, G.; Thomazeau, C.; Guisnet, M. Hydroisomerization and Hydrocracking of Alkanes. 7. Influence of the Balance between Acid and Hydrogenating Functions on the Transformation of *n*-Decane on PtHY Catalysts. *J. Catal.* **1996**, *162*, 179–189.
15. de Graaf, J.; van Dillen, A. J.; de Jong, K. P.; Koningsberger, D. C. Preparation of Highly Dispersed Pt Particles in Zeolite Y with a Narrow Particle Size Distribution: Characterization by Hydrogen Chemisorption, TEM, EXAFS Spectroscopy, and Particle Modeling. *J. Catal.* **2001**, *203*, 307–321.
16. Pandya, K. I.; Heald, S. M.; Hriljac, J. A.; Petrakis, L.; Fraissard, J. Characterization by EXAFS, NMR, and Other Techniques of Pt/NaY Zeolite at Industrially Relevant Low Concentration of Platinum. *J. Phys. Chem.* **1996**, *100*, 5070–5077.

17. Chmelka, B. F.; Went, G. T.; Csencsits, R.; Bell, A. T.; Petersen, E. E.; Radke, C. J. Oxidation of Reduced Pt Clusters in Pt-NaY. *J. Catal.* **1993**, *144*, 506–524.
18. Pan, M.; Cowley, J. M.; Chan, I. Y. HREM Imaging of Small Pt Clusters Dispersed in Y-Zeolites. *Catal. Lett.* **1990**, *5*, 1–12.
19. Kampers, F. W. H.; Engelen, C. W. R.; van Hooff, J. H. C.; Koningsberger, D. C. Influence of Preparation Method on the Metal Cluster Size of Pt/ZSM-5 Catalysts As Studied with Extended X-ray Absorption Fine Structure Spectroscopy. *J. Phys. Chem.* **1990**, *94*, 8574–8578.
20. Tzou, M. S.; Teo, B. K.; Sachtler, W. M. H. Formation of Pt Particles in Y-Type Zeolites. The Influence of Coexchanged Metal Cations. *J. Catal.* **1988**, *113*, 220–235.
21. Reagan, W. J.; Chester, A. W.; Kerr, G. T. Studies of the Thermal Decomposition and Catalytic Properties of Some Platinum and Palladium Ammine Zeolites. *J. Catal.* **1981**, *69*, 89–100.
22. Gallezot, P.; Alarcon-Diaz, A.; Dalmon, J.-A.; Renuoprez, A. J.; Imelik, B. Location and Dispersion of Platinum in PtY Zeolites. *J. Catal.* **1975**, *39*, 334–349.
23. Buurmans, I. L. C.; Weckhuysen, B. M. Heterogeneities of Individual Catalyst Particles in Space and Time as Monitored by Spectroscopy. *Nat. Chem.* **2012**, *4*, 873–886.
24. Koster, A. J.; Ziese, U.; Verkleij, A. J.; Janssen, A. H.; de Jong, K. P. Three-Dimensional Transmission Electron Microscopy: A Novel Imaging and Characterization Technique with Nanometer Scale Resolution for Materials Science. *J. Phys. Chem. B* **2000**, *104*, 9368–9370.
25. Ersen, O.; Werckmann, J.; Houllé, M.; Ledoux, M.-J.; Pham-Huu, C. 3D Electron Microscopy Study of Metal Particles Inside Multiwalled Carbon Nanotubes. *Nano Lett.* **2007**, *7*, 1898–1907.
26. Friedrich, H.; Sietsma, J. R. A.; de Jongh, P. E.; Verkleij, A. J.; de Jong, K. P. Measuring Location, Size, Distribution, and Loading of NiO Crystallites in Individual SBA-15 Pores by Electron Tomography. *J. Am. Chem. Soc.* **2007**, *129*, 10249–10254.
27. Ward, E. W. P.; Yates, T. J. V.; Fernández, J.-J.; Vaughan, D. E. W.; Midgley, P. A. Three-Dimensional Nanoparticle Distribution and Local Curvature of Heterogeneous Catalysts Revealed by Electron Tomography. *J. Phys. Chem. C* **2007**, *111*, 11501–11505.
28. Arslan, I.; Walmsley, J. C.; Rytter, E.; Bergene, E.; Midgley, P. A. Toward Three-Dimensional Nanoengineering of Heterogeneous Catalysts. *J. Am. Chem. Soc.* **2008**, *130*, 5716–5719.
29. Florea, I.; Houllé, M.; Ersen, O.; Roiban, L.; Deneuve, A.; Janowska, I.; Nguyen, P.; Pham, C.; Pham-Huu, C. Selective Deposition of Palladium Nanoparticles inside the Bimodal Porosity of β-SiC Investigated by Electron Tomography. *J. Phys. Chem. C* **2009**, *113*, 17711–17719.
30. Bals, S.; Batenburg, K. J.; Liang, D.; Lebedev, O.; Van Tendeloo, G.; Aerts, A.; Martens, J. A.; Kirschhock, C. E. A. Quantitative Three-Dimensional Modeling of Zeotile through Discrete Electron Tomography. *J. Am. Chem. Soc.* **2009**, *131*, 4769–4773.
31. Friedrich, H.; de Jongh, P. E.; Verkleij, A. J.; de Jong, K. P. Electron Tomography for Heterogeneous Catalysts and Related Nanostructured Materials. *Chem. Rev.* **2009**, *109*, 1613–1629.
32. Nan, F.; Song, C.; Zhang, J.; Hui, R.; Chen, J.; Fairbridge, C.; Botton, G. A. STEM HAADF Tomography of Molybdenum Disulfide with Mesoporous Structure. *ChemCatChem* **2011**, *3*, 999–1003.
33. Gommes, C. J.; Friedrich, H.; Wolters, M.; de Jongh, P. E.; de Jong, K. P. Quantitative Characterization of Pore Corrugation in Ordered Mesoporous Materials Using Image Analysis of Electron Tomograms. *Chem. Mater.* **2009**, *21*, 1311–1317.
34. Friedrich, H.; Guo, S.; de Jongh, P. E.; Pan, X.; Bao, X.; de Jong, K. P. A Quantitative Electron Tomography Study of Ruthenium Particles on the Interior and Exterior Surfaces of Carbon Nanotubes. *ChemSusChem* **2011**, *4*, 957–963.
35. Georgescu, D.; Roiban, L.; Ersen, O.; Ihiawakrim, D.; Baia, L.; Simon, S. Insights on Ag Doped Porous TiO$_2$ Nanostructures: A Comprehensive Study of Their Structural and Morphological Characteristics. *RSC Adv.* **2012**, *2*, 5358–5369.

36. Leary, R.; Saghi, Z.; Armbrüster, M.; Wowsnick, G.; Schlögl, R.; Thomas, J. M.; Midgley, P. A. Quantitative High-Angle Annular Dark-Field Scanning Transmission Electron Microscope (HAADF-STEM) Tomography and High-Resolution Electron Microscopy of Unsupported Intermetallic GaPd$_2$ Catalysts. *J. Phys. Chem. C* **2012**, *116*, 13343–13352.

37. Leary, R.; Midgley, P. A.; Thomas, J. M. Recent Advances in the Application of Electron Tomography to Materials Chemistry. *Acc. Chem. Res.* **2012**, *45*, 1782–1791.

38. Zečević, J.; Gommes, C. J.; Friedrich, H.; de Jongh, P. E.; de Jong, K. P. Mesoporosity of Zeolite Y: Quantitative Three-Dimensional Study by Image Analysis of Electron Tomograms. *Angew. Chem., Int. Ed.* **2012**, *51*, 4213–4217.

39. Florea, I.; Demortière, A.; Petit, C.; Bulou, H.; Hirlimann, C.; Ersen, O. 3D Quantitative Analysis of Platinum Nanocrystal Superlattices by Electron Tomography. *ACS Nano* **2012**, *6*, 2574–2581.

40. Goris, B.; Bals, S.; Van den Broek, W.; Carbó-Argibay, E.; Gómez-Graña, S.; Liz-Marzán, L. M.; Van Tendeloo, G. Atomic-Scale Determination of Surface Facets in Gold Nanorods. *Nat. Mater.* **2012**, *11*, 930–935.

41. Prieto, G.; Zečević, J.; Friedrich, H.; de Jong, K. P.; de Jongh, P. E. Towards Stable Catalysts by Controlling Collective Properties of Supported Metal Nanoparticles. *Nat. Mater.* **2013**, *12*, 34–39.

42. van Donk, S.; Janssen, A. H.; Bitter, J. H.; de Jong, K. P. Generation, Characterization, and Impact of Mesopores in Zeolite Catalysts. *Catal. Rev.: Sci. Eng.* **2003**, *45*, 297–319.

43. Verboekend, D.; Vilé, G.; Pérez-Ramírez, J. Hierarchical Y and USY Zeolites Designed by Post-synthetic Strategies. *Adv. Funct. Mater.* **2012**, *22*, 916–928.

44. Janssen, A. H.; Koster, A. J.; de Jong, K. P. Three-Dimensional Transmission Electron Microscopic Observations of Mesopores in Dealuminated Zeolite Y. *Angew. Chem., Int. Ed.* **2001**, *40*, 1102–1104.

45. de Jong, K. P.; Zečević, J.; Friedrich, H.; de Jongh, P. E.; Bulut, M.; van Donk, S.; Kenmogne, R.; Finiels, A.; Hulea, V.; Fajula, F. Zeolite Y Crystals with Trimodal Porosity as Ideal Hydrocracking Catalysts. *Angew. Chem., Int. Ed.* **2010**, *49*, 10074–10078.

46. Philippaerts, A.; Paulussen, S.; Turner, S.; Lebedev, O. I.; Van Tendeloo, G.; Poelman, H.; Bulut, M.; De Clippel, F.; Smeets, P.; Sels, B.; *et al.* Selectivity in Sorption and Hydrogenation of Methyl Oleate and Elaidate on MFI Zeolites. *J. Catal.* **2010**, *270*, 172–184.

47. Bovin, J.-O.; Alfredsson, V.; Karlsson, G.; Carlsson, A.; Blum, Z.; Terasaki, O. TEM-Tomography of FAU-Zeolite Crystals Containing Pt-Clusters. *Ultramicroscopy* **1996**, *62*, 277–281.

48. Zečević, J.; van der Eerden, A. M. J.; Friedrich, H.; de Jongh, P. E.; de Jong, K. P. H$_2$PtCl$_6$-Derived Pt Nanoparticles on USY Zeolite: A Qualitative and Quantitative Electron Tomography Study. *Microporous Mesoporous Mater.* **2012**, *164*, 99–103.

49. Kremer, J. R.; Mastronarde, D. N.; McIntosh, J. R. Computer Visualization of Three-Dimensional Image Data Using IMOD. *J. Struct. Biol.* **1996**, *116*, 71–76.